Nano-Micro Letters

ISSN 2311-6706
e-ISSN 2150-5551
CN 31-2103/TB

ARTICLE

https://doi.org/10.1007/s40820-019-0242-8

Cite as
Nano-Micro Lett.
(2019) 11:12

Received: 15 December 2018
Accepted: 14 January 2019
Published online: 5 February 2019

High-Index-Faceted Ni_3S_2 Branch Arrays as Bifunctional Electrocatalysts for Efficient Water Splitting

Shengjue Deng[1], Kaili Zhang[1], Dong Xie[2], Yan Zhang[1], Yongqi Zhang[3], Yadong Wang[4], Jianbo Wu[5], Xiuli Wang[1], Hong Jin Fan[3], Xinhui Xia[1] ✉, Jiangping Tu[1] ✉

Shengjue Deng and Kaili Zhang contributed equally to this work.

✉ Xinhui Xia, helloxxh@zju.edu.cn; Jiangping Tu, tujp@zju.edu.cn

[1] State Key Laboratory of Silicon Materials, Key Laboratory of Advanced Materials and Applications for Batteries of Zhejiang Province, and Department of Materials Science and Engineering, Zhejiang University, Hangzhou 310027, People's Republic of China

[2] Guangdong Engineering and Technology Research Center for Advanced Nanomaterials, School of Environment and Civil Engineering, Dongguan University of Technology, Dongguan 523808, People's Republic of China

[3] School of Physical and Mathematical Sciences, Nanyang Technological University, Singapore 637371, Singapore

[4] School of Engineering, Nanyang Polytechnic, Singapore 569830, Singapore

[5] Zhejiang Provincial Key Laboratory for Cutting Tools, Taizhou University, Taizhou 318000, People's Republic of China

HIGHLIGHTS

- TiO_2@Ni_3S_2 core/branch arrays are constructed via a low-temperature sulfurization.
- Highly active $\{\bar{2}10\}$ high-index facet of Ni_3S_2 is exposed for both oxygen evolution reaction (OER) and hydrogen evolution reaction (HER).
- Remarkable bifunctional electrocatalytic activity is observed for both HER and OER.

ABSTRACT For efficient electrolysis of water for hydrogen generation or other value-added chemicals, it is highly relevant to develop low-temperature synthesis of low-cost and high-efficiency metal sulfide electrocatalysts on a large scale. Herein, we construct a new core–branch array and binder-free electrode by growing Ni_3S_2 nanoflake branches on an atomic-layer-deposited (ALD) TiO_2 skeleton. Through induced growth on the ALD-TiO_2 backbone, cross-linked Ni_3S_2 nanoflake branches with exposed $\{\bar{2}10\}$ high-index facets are uniformly anchored to the preformed TiO_2 core forming an integrated electrocatalyst. Such a core–branch array structure possesses large active surface area, uniform porous structure, and rich active sites of the exposed $\{\bar{2}10\}$ high-index facet in the Ni_3S_2 nanoflake. Accordingly, the TiO_2@Ni_3S_2 core/branch arrays exhibit remarkable electrocatalytic activities in an alkaline medium, with lower overpotentials for both oxygen evolution reaction (220 mV at 10 mA cm^{-2}) and hydrogen evolution reaction (112 mV at 10 mA cm^{-2}), which are better than those of other Ni_3S_2 counterparts. Stable overall water splitting based on this bifunctional electrolyzer is also demonstrated.

KEYWORDS Nickel sulfide; Core/branch arrays; Porous film; Bifunctional electrocatalysts; Electrochemical water splitting; Oxygen evolution reaction (OER); Hydrogen evolution reaction (HER)

1 Introduction

Production of hydrogen/oxygen fuels through electrochemical water splitting is considered one of the most efficient green technologies, although large-scale synthesis of cost-effective electrocatalysts used in this process still remains a huge challenge [1–5]. Platinum (Pt)/Pt-based alloys and iridium/ruthenium oxides (IrO_2/RuO_2) are regarded as the most efficient electrocatalysts for electrochemical hydrogen evolution reaction (HER) and oxygen evolution reaction (OER), respectively [6–10]. However, their high cost and compromised stability as well as the low earth abundance of these metals impede their widespread application [11–15]. Therefore, it is highly desirable to fabricate alternative noble-metal-free and durable electrocatalysts for both OER and HER systems. Although transition metal oxides and hydroxides (NiO, CoO, $Ni(OH)_2$, etc.) [16] are being widely investigated, they mostly have intrinsically low electrical conductivity and their composites with carbon additives should be prepared to improve the electrical conductivity. Metal sulfides, such as nickel sulfide (Ni_3S_2), are more attractive candidates for electrochemical water splitting, owing to their intrinsic high conductivity, rich catalytic activity, and superior electrochemical stability when applied in HER/OER [17, 18]. Currently, a wide range of nanostructured Ni_3S_2 (such as Fe-doped Ni_3S_2 [19] and nanorods [20]) and composites (e.g., Ni_3S_2 nanosheets/Ni [21], Ni_3S_2 nanotube/Ni [18]) has been prepared by different methods. They demonstrate improved performance in HER or OER owing to increased exposure of the active sites and boosted ion/electron transfer. Despite these efforts, the overall water-splitting activity of the same Ni_3S_2-based catalysts for both HER and OER has been rarely reported. In addition, the aforementioned Ni_3S_2 electrocatalysts are usually synthesized via chemical vapor deposition (CVD) and hydrothermal methods. However, these methods require high-temperature treatment or the use of polluted thiourea or trithiocyanuric acid. Moreover, the high-temperature treatment may cause the coverage or loss of the active sites of Ni_3S_2 [22–25]. In this context, a facile and green low-temperature synthesis method for Ni_3S_2 electrocatalysts is highly desirable.

Low-temperature (< 100 °C) sulfurization using a Na_2S solution is a green way for the large-scale synthesis of nanostructured metal sulfides owing to easy processing, high efficiency, and cost-effectiveness. Moreover, this method is particularly suitable for the direct synthesis of metal sulfides arrays with tailored nanostructures. Meanwhile, it has been demonstrated that a high-index-faceted Ni_3S_2 nanosheet could have superior HER activity owing to possible synergistic catalytic effects arising from the nanosheet array and the exposed $\{\bar{2}10\}$ high-index facets [26]. Inspired by these encouraging results, we set out to employ a low-temperature synthesis route to produce Ni_3S_2 nanoarrays with preferentially exposed $\{\bar{2}10\}$ high-index facets as a binder-free electrocatalyst. In addition, in order to further increase the areal load of the active material, we aimed to grow the Ni_3S_2 arrays as branches on a conductive scaffold to form a core–branch array structure, instead of directly depositing them on carbon cloth.

Herein, we report a facile low-temperature (< 100 °C) sulfurization strategy to synthesize large-scale TiO_2@Ni_3S_2 core/branch arrays as a binder-free electrode for a water-splitting electrolyzer in an alkaline solution. An induced growth process for growing Ni_3S_2 nanobranch on a TiO_2 core obtained by atomic layer deposition (ALD) is proposed, which leads to the in situ growth of $\{\bar{2}10\}$ high-index facets of Ni_3S_2. The as-prepared TiO_2@Ni_3S_2 core/branch arrays possess large active areas, uniform porous structures, and rich active sites of the exposed $\{\bar{2}10\}$ high-index facet. These features lead to substantial enhancements in HER and OER activities compared to those of most of the reported Ni_3S_2-based catalysts. Low overpotentials and fast kinetics as well as superior long-term durability of TiO_2@Ni_3S_2 core/branch arrays are demonstrated. A low-water-splitting voltage of 1.58 V at 10 mA cm^{-2} is obtained upon using the TiO_2@Ni_3S_2 array electrode as both a cathode and an anode. Our new electrode design strategy paves a green way for the construction of large-scale nickel sulfides with high electrocatalytic efficiency for electrochemical energy storage and conversion applications.

2 Experimental

2.1 Material Synthesis

In the first step, $Ni_2(OH)_2CO_3$ nanosheet arrays were obtained by a one-step hydrothermal method using commercial nickel foam as the substrate. For this, $Ni(NO_3)_2$ (0.9 g), NH_4F (0.23 g), and urea (0.9 g) were dissolved in 75 mL of

https://doi.org/10.1007/s40820-019-0242-8

deionized (DI) water to form a reaction solution. Then, the solution was transferred to a Teflon-lined steel autoclave, and the autoclave was placed in an oven at 120 °C for 8 h. After natural cooling, the sample was rinsed thoroughly with DI water.

In order to synthesize TiO_2@$Ni_2(OH)_2CO_3$ nanoflake arrays, the prepared $Ni_2(OH)_2CO_3$ nanosheet arrays were placed in an ALD reactor (ALD PICOSUN P-300F) along with $TiCl_4$ and H_2O as the Ti and O source, respectively. Then, TiO_2 was deposited at 120 °C for 140 cycles. Argon was used as the carrier gas. The final step was the sulfurization process. Typically, the obtained TiO_2@$Ni_2(OH)_2CO_3$ nanoflake array samples were transferred to a 0.1 M Na_2S solution and heated at 90 °C for 9 h. After natural cooling and rinsing with DI water, the TiO_2@Ni_3S_2 core/branch arrays were obtained. For comparison, Ni_3S_2 nanoflake arrays were also synthesized by the direct sulfurization of the $Ni_2(OH)_2CO_3$ nanosheet arrays on nickel foam (without the ALD TiO_2 step) using the same sulfurization conditions mentioned above.

2.2 Material Characterization

Morphologies and microstructures of all samples were investigated using a field-emission scanning electron microscope (FESEM, Hitachi SU8010) and a transmission electron microscope (TEM, JEOL 2100F). The crystal structure was characterized by X-ray diffraction (XRD) with Cu Kα radiation (RigakuD/Max-2550). Raman spectra were collected using a Renishaw-inVia Raman microscope with 514-nm laser excitation. X-Ray photoelectron spectroscopy was performed on an ESCALAB_250Xi X-Ray photoelectron spectrometer with an Al Kα source. Specific surface area distributions were obtained using a porosity instrument (BET, JW-BK112).

2.3 Electrochemical Measurements

HER and OER experiments were conducted using an electrochemical workstation (CH Instrument 660D) with a standard three-electrode setup at room temperature; the as-prepared samples, carbon rod ($D = 8$ mm), and saturated calomel electrode were used as the working electrode, counter electrode, and reference electrode, respectively. A 1 M KOH solution was used as the electrolyte for both HER and OER tests. All potentials in this work are referred to the reversible hydrogen electrode. All measurements were first carried out following a cyclic voltammetry (CV) test at 100 mV s^{-1} to stabilize the current. Linear sweep voltammetry (LSV) tests were performed at a scan rate of 5 mV s^{-1}. The Tafel plots of the samples were obtained from the LSV curves acquired with a scan rate of 1 mV s^{-1}. Electrochemical impedance spectroscopy (EIS) was performed at the polarization voltage being indexed to the current density of 10 mA cm^{-2}, in the frequency range of 100 kHz to 50 mHz with an AC amplitude of 10 mV. The stability test was carried out after 10,000 CV cycles. These results were obtained by iR compensation. The overall water splitting was performed in a two-electrode catalyzer, where two pieces of TiO_2@Ni_3S_3 samples with a geometric area of 1 cm^2 were used as the electrodes for HER and OER.

3 Results and Discussion

3.1 Physicochemical Properties of TiO_2@Ni_3S_2 Core/Branch Arrays

The core/branch structure of the TiO_2@Ni_3S_2 arrays is schematically illustrated in Fig. 1a. $Ni_2(OH)_2CO_3$ nanoflake arrays were synthesized on commercial nickel foam via a standard hydrothermal process (see details in Sect. 2.1). A TiO_2 layer with 10 nm thickness was deposited on the surface of the $Ni_2(OH)_2CO_3$ nanoflakes using a simple ALD method. The obtained TiO_2@$Ni_2(OH)_2CO_3$ arrays were converted to TiO_2@Ni_3S_2 core/branch arrays by immersing them into a Na_2S solution and heated. We applied this unique-structured material as electrocatalyst and propose the following advantages in enhancing the HER and OER:

1. Branched Ni_3S_2 nanoflakes possess a high surface area and higher porosity than those of the pure Ni_3S_2 nanoflakes grown directly on Ni foam. Further, the open structure of the interconnected nanoflakes will facilitate ion diffusion and H_2/O_2 detachment during the HER/OER processes. This is particularly beneficial for large-current electrocatalysis.
2. The ALD-TiO_2 skeleton not only serves a mechanical support for the Ni_3S_2 branch, but also induces the nucleation for the directional growth of Ni_3S_2. Without the ALD-TiO_2 skeleton, no Ni_3S_2-branch can be formed. The TiO_2 and Ni_3S_2 act synergistically to provide better mechanical stability and enhanced specific surface area and larger porosity [27, 28].

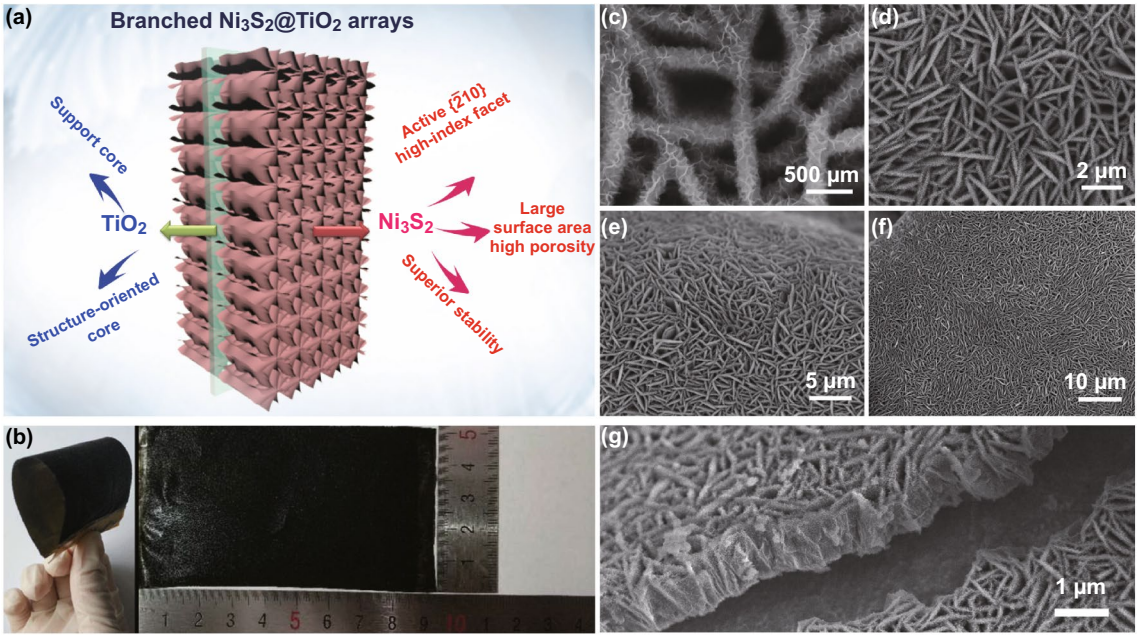

Fig. 1 **a** Schematic illustration of the core/branch structure of the TiO_2@Ni_3S_2 arrays. **b** Optical photograph of the sample. **c**–**g** SEM images of the TiO_2@Ni_3S_2 core/branch arrays

3. One important feature of this unique branched Ni_3S_2 nanoflakes is the exposure of their highly active {$\bar{2}$10} high-index facets, which can further improve the HER/OER activities leading to a lower overpotential and Tafel slope.

The morphological evolution of the samples at different stages of the synthesis is revealed by the SEM images (see Fig. S1). The hydrothermally synthesized $Ni_2(OH)_2CO_3$ nanoflakes with thicknesses between 40 and 60 nm are found aligned vertically on the nickel foam surface, forming an architecture with a porous network (Fig. S1a, b). After the ALD of TiO_2, the twisted nanoflakes of $Ni_2(OH)_2CO_3$ smoothened to form TiO_2@$Ni_2(OH)_2CO_3$ core/shell arrays. Further, the thickness of the TiO_2@$Ni_2(OH)_2CO_3$ core/shell arrays increased to 50–70 nm. However, the 3D porous structure is still preserved, which is not surprising since the ALD generally results in a uniform and conformal deposition of a smooth thin film of amorphous TiO_2 (Fig. S1c, d). However, after the final sulfurization in Na_2S solution at 90 °C, the morphology changed radically; the previous core/shell structure of TiO_2@$Ni_2(OH)_2CO_3$ transformed into a new type of branched structure of TiO_2@Ni_3S_2. It is observed that the TiO_2@Ni_3S_2 sample is black and the display area is ~45 cm^2. This process can be easily adapted for large-scale production (Fig. 1b). Meanwhile, the internal TiO_2 core is homogeneously coated by the cross-linked Ni_3S_2 nanoflake shell with 10–15 nm thickness (Fig. 1c, f). Furthermore, the porous morphology remained well preserved in the TiO_2@Ni_3S_2 core/branch arrays. These unique porous structural features provide a number of tunnels to boost electron/ion transfer. As shown in Fig. 1g, the TiO_2@Ni_3S_2 core/branch arrays grew quasi-vertically with respect to the substrate with a height of ~ 1 μm.

The branched microstructure of the TiO_2@Ni_3S_2 arrays was also explored by TEM observation. The $Ni_2(OH)_2CO_3$ nanoflake presents a thin and smooth appearance (Fig. S2a). The measured interplanar *d*-spacing of $Ni_2(OH)_2CO_3$ is about 0.26 nm, which corresponds well with that of the (−201) plane of $Ni_2(OH)_2CO_3$ (JCPDS 35-0501) (Fig. S2b) [29]. After the ALD of TiO_2, the $Ni_2(OH)_2CO_3$ is completely coated with a thin layer of TiO_2 with ~ 10 nm thickness (Fig. S2c, d), forming a TiO_2@$Ni_2(OH)_2CO_3$ core/shell structure. Additionally, the thin TiO_2 is amorphous in nature and the interplanar *d*-spacing of 0.26 nm is still noticed for $Ni_2(OH)_2CO_3$. As for the TiO_2@Ni_3S_2 sample, the pristine TiO_2@$Ni_2(OH)_2CO_3$ core/shell structure changed to core/branch array, in which the TiO_2 core is homogeneously covered by cross-linked Ni_3S_2 nanoflakes (Fig. 2a). A clear interplanar *d*-spacing of ~ 0.71 nm is observed, which may

 https://doi.org/10.1007/s40820-019-0242-8

be due to the expansion of the *c* axis of Ni_3S_2. In addition, the selected area electron diffraction (SAED) pattern shows polycrystalline diffraction rings of the TiO_2@Ni_3S_2 sample (Fig. 2b), which is in good agreement with the (001), (101), (110), and (021) planes of Ni_3S_2.

HRTEM investigation was performed along the [100] zone axis of Ni_3S_2, and interestingly, the interplanar *d*-spacing of 0.24 and 0.23 nm matched well with the (003) and (021) planes of the hexagonal Ni_3S_2 phase (JCPDS 44-1418). Further, the angle between the (003) and (021) facets is approximately 70°, which corresponds to the theoretical value of 70.8° (Fig. 2c, d). This implies that the exposed facets of the Ni_3S_2 nanoflakes are $\{\bar{2}10\}$ high-index facets. According to a previous report by Fang et al. [26], this facet shows superior catalytic performance. Energy-dispersive X-ray spectroscopy (EDS) maps (Fig. 2e) confirm the presence and uniform distribution of O, S, Ni, and Ti in the TiO_2@Ni_3S_2 arrays.

In our experiment, the ALD-TiO_2 skeleton serves as a nucleation core for the directional growth of Ni_3S_2 nanosheets. Without the ALD-TiO_2 skin, no Ni_3S_2 branch can be formed. Comparatively, only common Ni_3S_2 nanoflake arrays are

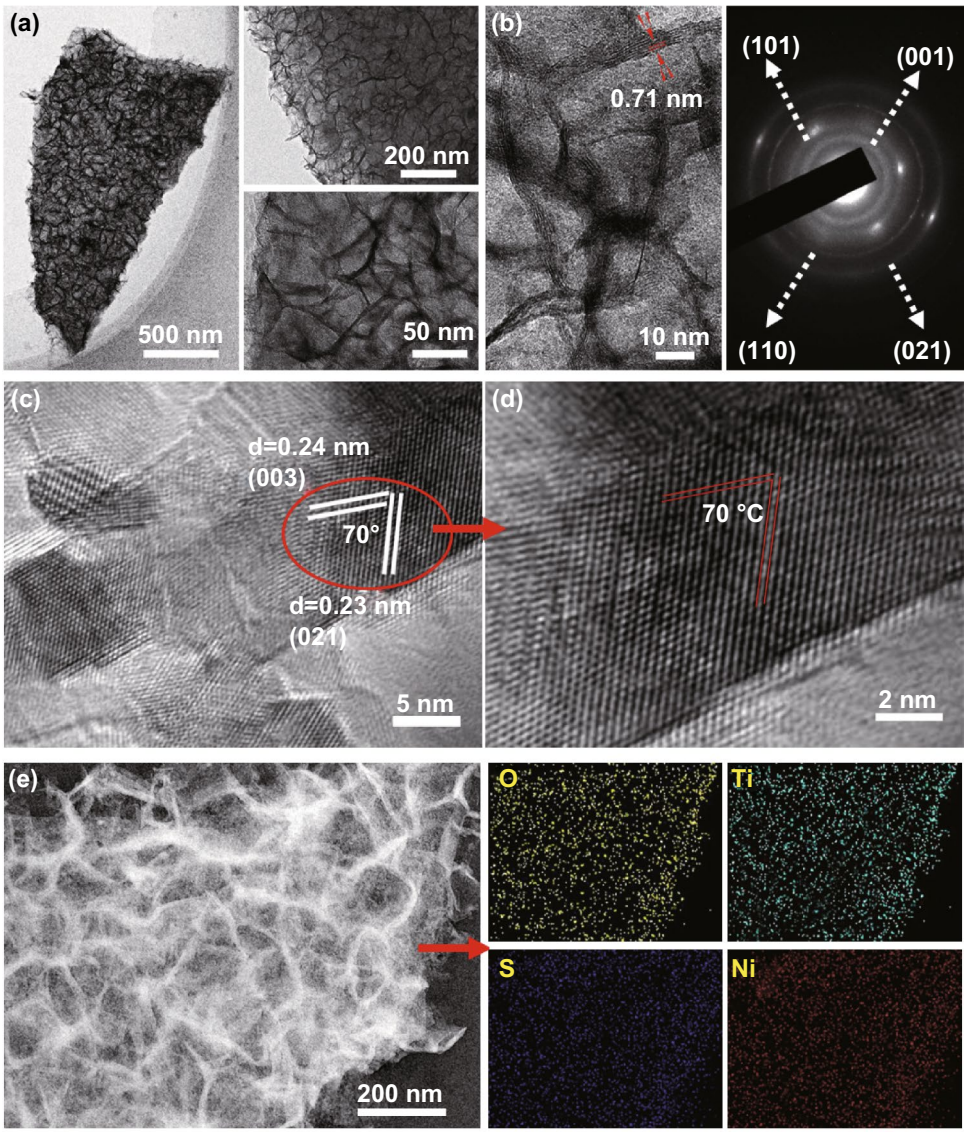

Fig. 2 **a–d** TEM-HRTEM images and SAED pattern of TiO_2@Ni_3S_2 core/branch arrays. **e** EDS elemental maps of O, S, Ni, and Ti in TiO_2@Ni_3S_2 core/branch arrays

formed in the absence of the TiO_2 layer support (Fig. S3a, b). Interestingly, exposed {$\bar{2}$10} facets are also found in common Ni_3S_2 nanosheet arrays, indicating that the low-temperature sulfurization method is favorable for the growth of the high-index {$\bar{2}$10} facet, which is also confirmed by TEM and XRD (Fig. S3c, d). During the sulfurization process, the Ni ions would diffuse outward and combine with sulfur-containing groups (S^{2-}, HS^-, etc.) along the outer surface of ALD-TiO_2 to form Ni_3S_2 nanocrystal nuclei. This outward diffusion process might be related to the Ostwald ripening effect, in which the energy of the interior is higher than that on outer surface. Ni_3S_2 species are spontaneously attached to the ALD-TiO_2 surface, which induces the growth of active nucleation centers and decreases the interfacial energy barrier for the self-assembly of the Ni_3S_2 nanoflake branches.

To further demonstrate the benefits of the core/branch arrays, the specific surface area was determined by BET (Fig. S4). The common Ni_3S_2 arrays and TiO_2@Ni_3S_2 branch nanosheet arrays show specific surface areas of 1.594 and 4.623 $m^2\ g^{-1}$, respectively, implying that branching leads to significantly increased surface area. Furthermore, the branched nanoflakes are beneficial in that they provide increased exposed active area/sites, leading to increased utilization of the active Ni_3S_2 catalyst.

In order to identify the phase and composition of the final product, XRD, Raman spectroscopy, and XPS were carried out. Figures S5 and 3a show the typical XRD patterns of $Ni_2(OH)_2CO_3$, TiO_2@$Ni_2(OH)_2CO_3$, and TiO_2@Ni_3S_2. Except for the diffraction peaks of Ni foam, other diffraction peaks in the XRD pattern of $Ni_2(OH)_2CO_3$ correspond well with those of the monoclinic $Ni_2(OH)_2CO_3$ phase (JCPDS 35-0501), suggesting the high crystallinity of $Ni_2(OH)_2CO_3$. For the TiO_2/$Ni_2(OH)_2CO_3$ arrays, the diffraction peaks of $Ni_2(OH)_2CO_3$ can be still detected, but the strength of them decreases. No peaks of the TiO_2 are noticed, indicating the amorphous nature of the TiO_2 skeleton (Fig. S5). After the low-temperature sulfurization using the Na_2S solution, the diffraction peaks of $Ni_2(OH)_2CO_3$ disappear, and other diffraction peaks that can be indexed well with the Ni_3S_2 phase (JCPDS 44-1418) are observed apart from the peaks of metallic Ni foam substrate, demonstrating that the as-obtained TiO_2@Ni_3S_2 sample is of high purity [30]. It is worth noting that the strong diffraction peaks of (021) and (003) plane can be observed clearly (Fig. 3a). Meanwhile, the Raman analysis further confirms the formation of the TiO_2@Ni_3S_2 phase. The TiO_2@Ni_3S_2 arrays show five characteristic peaks at ~ 203, 223, 305, and 348 cm^{-1}, which match well with those of the Ni_3S_2 phase. The characteristic peak at ~ 150 cm^{-1} could be indexed well with that of amorphous TiO_2 (Fig. 3b) [1], further manifesting the successful preparation of TiO_2@Ni_3S_2 core/branch arrays. This conclusion is also supported by XPS results. Figure 3c shows the

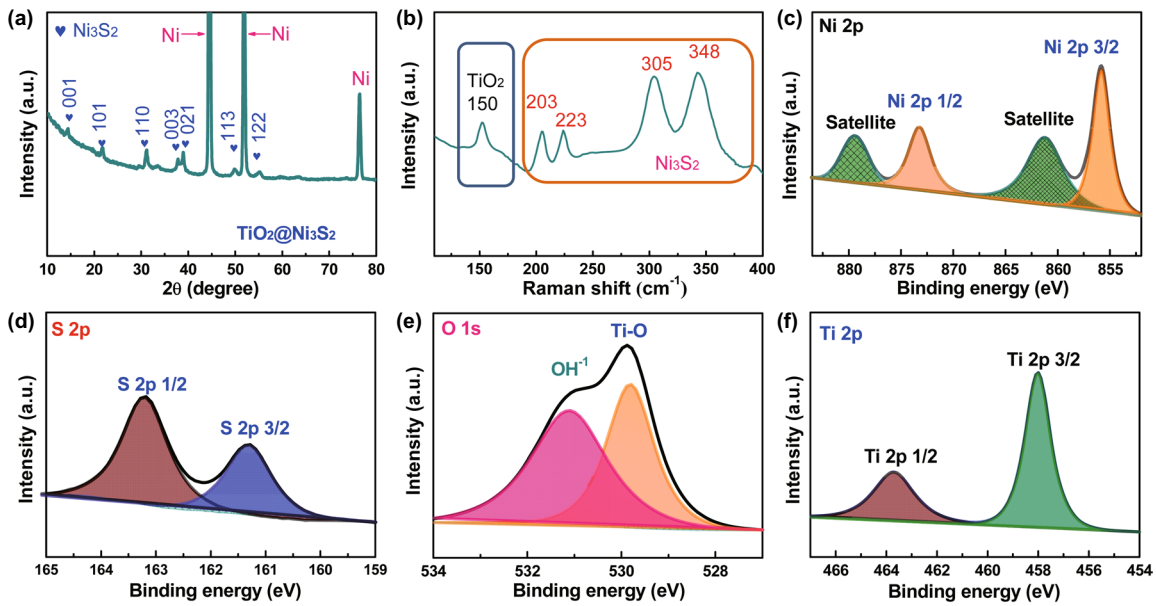

Fig. 3 **a** XRD patterns, **b** Raman spectrum, **c** core-level Ni 2*p* XPS spectra, **d** core-level S 2*p* XPS spectra, **e** O 1*s* XPS spectra, and **f** Ti 2*p* XPS spectra of TiO_2@Ni_3S_2 core/branch arrays

https://doi.org/10.1007/s40820-019-0242-8

high-resolution Ni 2*p* spectra of the TiO_2@Ni_3S_2 sample. Two main core levels (Ni 2*p*3/2 and Ni 2*p*1/2) that are characteristic of the Ni state in Ni_3S_2 are located at 873.28 and 855.78 eV, respectively [31]. As for the S 2*p* spectra, two characteristic peaks are detected at 163.28 eV (S 2*p*1/2) and 161.28 eV (S 2*p*3/2) corresponding to S^{2-} (Fig. 3d) [32]. Moreover, the presence of TiO_2 in the TiO_2@Ni_3S_2 core/branch arrays is also confirmed by Ti 2*p* and O 1*s* spectra (Fig. 3e, f). Two core-level peaks are located at 529.8 and 531.1 eV in the O 1*s* spectra, which could be indexed well with Ti–O and O–H bonds, respectively [33, 34]. Ti 2*p*1/2 (463.8 5 eV) and Ti 2*p*3/2 (458.0 eV), the characteristic peaks of TiO_2 are observed in the Ti 2*p* spectra. The presence of O–H bond may be due to surface oxidation of Ni_3S_2 [35–37]. All these results mutually confirm the successful fabrication of TiO_2@Ni_3S_2 core/branch arrays via our powerful low-temperature sulfurization strategy.

3.2 Electrocatalytic Properties of TiO_2@Ni_3S_2 Core/Branch Arrays

The electrocatalytic activity of the three samples ($Ni_2(OH)_2CO_3$, Ni_3S_2, and TiO_2@Ni_3S_2 electrodes) was studied using a three-electrode system in a 1 M KOH solution [38–41]. As presented in Fig. 4a, significantly, the TiO_2@Ni_3S_2 electrode displays the best HER activity with the smallest overpotential (112 mV at the current density of 10 mA cm^{-2}), better than that of the $Ni_2(OH)_2CO_3$ nanoflake arrays (154 mV) and Ni_3S_2 (149 mV) nanoflake arrays at the current density of 10 mA cm^{-2}. Meanwhile, the TiO_2@Ni_3S_2 core/branch arrays also show a large current density with the lowest overpotential (177 mV at the current density of 100 mA cm^{-2}), superior to those of the $Ni_2(OH)_2CO_3$ (259 mV) and Ni_3S_2 (213 mV) counterparts. Additionally, the enhanced HER performance is further confirmed by the Tafel slopes (Fig. 4b) derived from the previous LSV curves. Obviously, the $Ni_2(OH)_2CO_3$ and Ni_3S_2 electrodes show large Tafel slopes (105 and 77 mV/decade), while the TiO_2@Ni_3S_2 electrode exhibits a substantially lower Tafel slope of 69 mV per decade. It is well accepted that a lower Tafel slope implies a faster HER rate. As a result, the TiO_2@Ni_3S_2 electrode leads to the fastest HER process.

Furthermore, the HER performance of our designed high-index faceted Ni_3S_2 nanoflake arrays is also excellent. It is well known that HER involves three principal steps including Tafel (30 mV per decade) reactions, Heyrovsky (40 mV per decade), and Volmer (120 mV per decade) mechanisms [42]. Hence, it can be inferred that the HER with Ni_3S_2 and TiO_2@Ni_3S_2 electrodes in the alkaline water splitting is based on the Volmer mechanism. Simultaneously, the long-cycle durability of electrocatalysts plays an important role in practical application. The electrochemical stability test of the TiO_2@Ni_3S_2 arrays was carried out continuously at the scan rate of 50 mV s^{-1} for 10,000 CV cycles. The LSV curves of the TiO_2@Ni_3S_2 electrode before and after 10,000 CV cycles of electrolysis nearly overlap with each other, suggesting the excellent stability of TiO_2@Ni_3S_2 electrode (Fig. S6a).

In order to further understand the origin of the superior HER activity of the TiO_2@Ni_3S_2 core/branch nanoflake arrays, the effective electrochemical active surface area (ECSA) of the three samples was calculated by determining the double-layer capacitance (C_{dl}) based on the CV results at different scan rates (Fig. S6b–d). The obtained current density is plotted as a function of scan rates in Fig. 4c. The ECSA value is considered to be linearly proportional to the C_{dl} value, equaling half the slope value. Notably, the TiO_2@Ni_3S_2 electrode possesses a high capacitance, up to 42 mF cm^{-2}, which is much higher than those of $Ni_2(OH)_2CO_3$ (24 mF cm^{-2}) and Ni_3S_2 (29 mF cm^{-2}) electrodes. The above results indicate that the TiO_2@Ni_3S_2 electrode has more exposed active sites. EIS tests were performed to further probe the electrochemical behavior during the HER process. Figure 4d exhibits the Nyquist plots of all electrodes. The semicircle represents the charge transfer resistance (R_{ct}) of the hydrogen evolution reaction. Remarkably, the TiO_2@Ni_3S_2 electrode shows the smallest R_{ct} value among the three electrodes, which suggests that it facilitates the fastest dynamics during HER. Moreover, the solution resistance (R_s) values of $Ni_2(OH)_2CO_3$, Ni_3S_2, and TiO_2@Ni_3S_2 electrodes are 1.49, 1.46, and 1.45 Ω, respectively. These findings further verify that TiO_2@Ni_3S_2 still possesses high electronic conductivity and charge transfer ability during the entire hydrogen evolution reaction. In addition, the TiO_2@Ni_3S_2 electrode also shows long-term durability with no decay after 10 h at a large current density of 100 mA cm^{-2} (Fig. 4e).

As shown in Fig. 5a, the electrolysis cell of the two-electrode system consists of the TiO_2@Ni_3S_2 electrocatalyst as both anode and cathode in 1 M KOH solution (denoted as TiO_2@Ni_3S_2 ‖ TiO_2@Ni_3S_2). Apart from the outstanding HER activity, the as-prepared TiO_2@Ni_3S_2 electrode also delivers excellent OER catalytic performance in the alkaline solution.

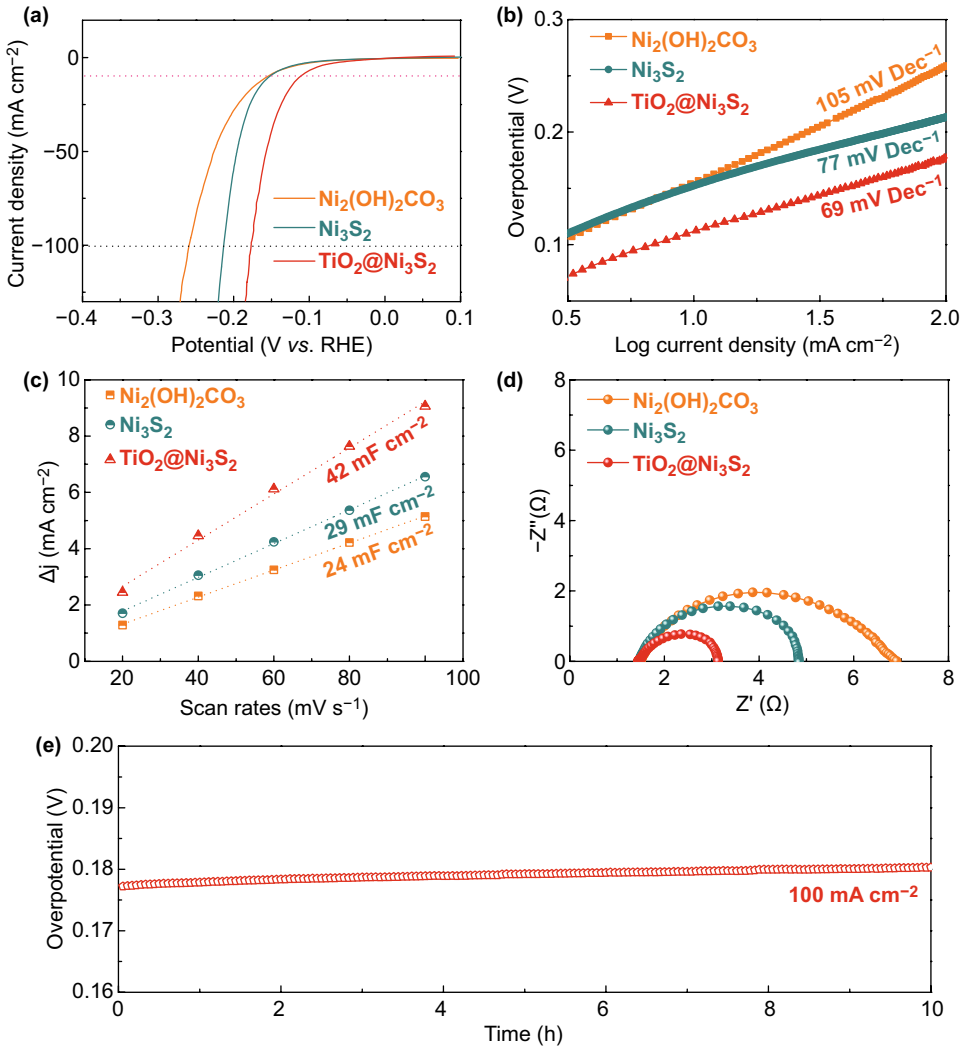

Fig. 4 Evaluation of the HER performance and comparison of $Ni_2(OH)_2CO_3$, Ni_3S_2, and TiO_2@Ni_3S_2 electrodes: **a** LSV curves, **b** Tafel plots, **c** current density as a function of scan rate, and **d** Nyquist plots of the $Ni_2(OH)_2CO_3$, Ni_3S_2, and TiO_2@Ni_3S_2 electrodes. **e** Electrochemical stability of the TiO_2@Ni_3S_2 electrode at a current density of 100 mA cm^{-2}

As shown in Fig. 5b, the TiO_2@Ni_3S_2 electrode exhibits a remarkably low OER overpotential of 220 mV at 10 mA cm^{-2} and 300 mV at 100 mA cm^{-2}, superior to those of the $Ni_2(OH)_2CO_3$ (330 mV, 390 mV) and Ni_3S_2 (280 mV, 360 mV) electrodes. Owing to its excellent catalytic activities in both OER and HER, the TiO_2@Ni_3S_2 electrode could be utilized as an attractive bifunctional electrocatalyst for water splitting in an alkaline medium. Impressively, a noticeably low cell voltage of 1.58 V is gained at the current density of 10 mA cm^{-2} (Fig. 5c), better than those of the other reported bifunctional electrocatalysts (Fig. 5d) [1, 9, 26, 43–47]. In order to investigate the change in the chemical composition of TiO_2@Ni_3S_2, high-resolution Ni 2*p* spectra were acquired after HER and OER tests (Fig. S7). After HER tests, the Ni 2*p* spectrum remained almost the same as before with a slight redshift owing to the cathodic H_2 reduction. However, after the OER test, the peak at 853.08 eV disappeared and the intensity of the satellite peak ($2p_{3/2}$) decreased because of the formation of hydrated nickel oxide. Furthermore, the TiO_2@Ni_3S_2 ‖ TiO_2@Ni_3S_2 catalyzer cell shows long-term durability with no decay after

https://doi.org/10.1007/s40820-019-0242-8

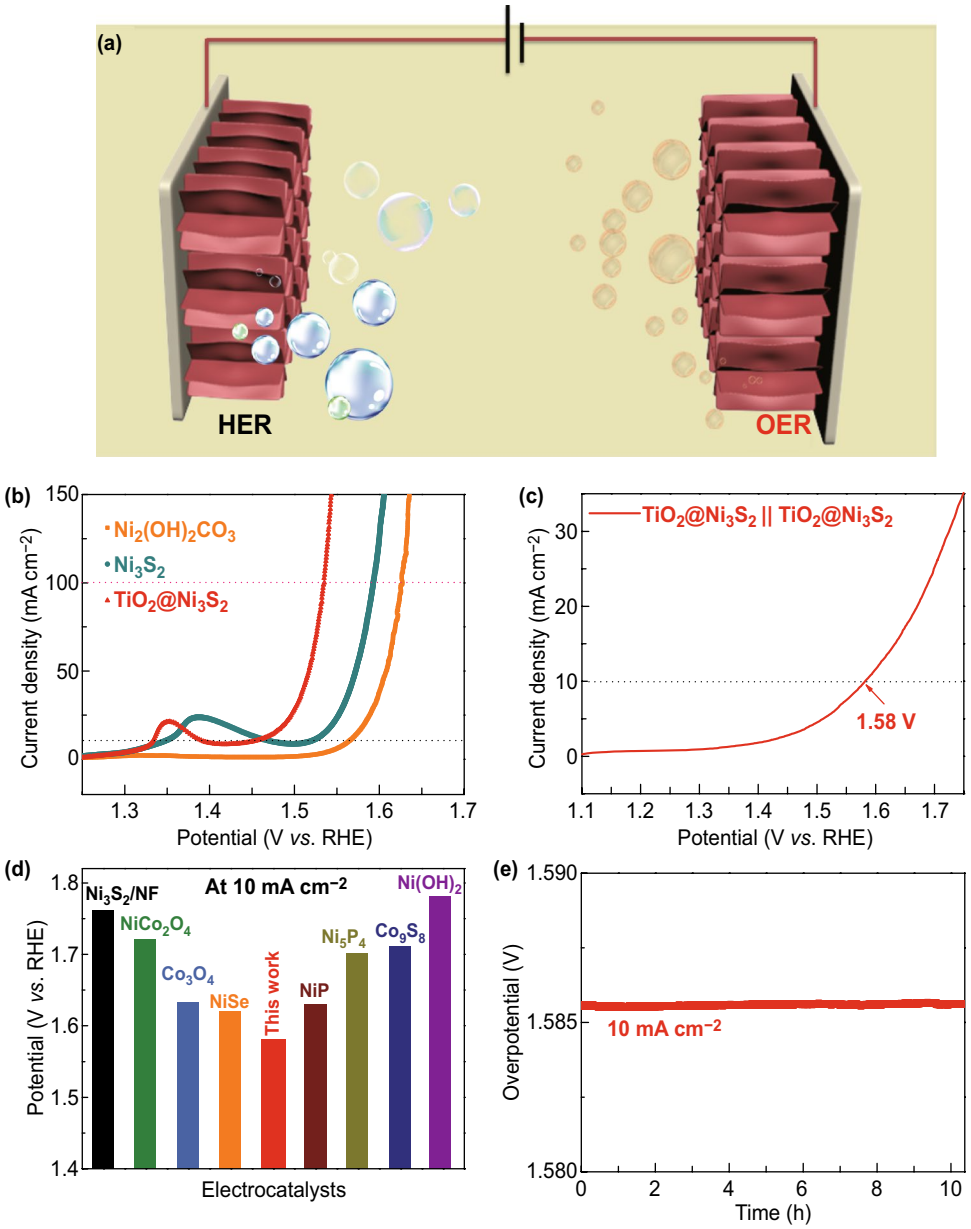

Fig. 5 **a** Schematic illustration of the overall water-splitting process using the bifunctional electrocatalyst. **b** LSV curves at 5 mV s^{-1} for the OER performances using the $Ni_2(OH)_2CO_3$, Ni_3S_2, and $TiO_2@Ni_3S_2$ electrodes. **c** LSV curves of the overall water-splitting performance of the $TiO_2@Ni_3S_2$||$TiO_2@Ni_3S_2$ electrolyzer. **d** Comparison of the overall water-splitting performance of our $TiO_2@Ni_3S_2$||$TiO_2@Ni_3S_2$ electrolyzer with those of other electrocatalysts in the literature, and **e** electrochemical stability at 10 mA cm^{-2}

10 h (Fig. 5c, e). All the above results demonstrate that the $TiO_2@Ni_3S_2$ core/branch arrays possess superior electrochemical activity in both HER and OER, suggesting that the designed $TiO_2@Ni_3S_2$ core/branch arrays would be promising electrocatalysts for practical application in alkaline water splitting.

4 Conclusion

We developed a facile and high-efficiency low-temperature sulfurization method for the large-scale synthesis of novel binder-free $TiO_2@Ni_3S_2$ core/branch arrays. Impressively, the as-obtained Ni_3S_2 nanoflake branches exposed the highly active $\{\bar{2}10\}$ high-index facet. Strong support and induced

directional growth of Ni_3S_2 nanoflakes are realized with the aid of the ALD-TiO_2 skeleton. Owing to large surface area of the core/branch arrays, large porosity, and binder-free adhesion as well as richer active sites of the exposed $\{\bar{2}10\}$ high-indexed facets of Ni_3S_2 nanoflakes, the designed TiO_2@Ni_3S_2 core/branch arrays deliver low overpotentials and Tafel slopes for both OER and HER as well as cycling stability in an alkaline medium superior to those of the other Ni_3S_2 counterparts. Our work offers a facile low-temperature strategy to construct advanced metal sulfide catalysts for electrochemical energy conversion and storage.

Acknowledgements This work is supported by National Natural Science Foundation of China (Grant Nos. 51728204 and 51772272), Fundamental Research Funds for the Central Universities (Grant No. 2018QNA4011), Qianjiang Talents Plan D (QJD1602029), Startup Foundation for Hundred-Talent Program of Zhejiang University, and the Fundamental Research Funds for the Central Universities (2015XZZX010-02).

Electronic supplementary material The online version of this article (https://doi.org/10.1007/s40820-019-0242-8) contains supplementary material, which is available to authorized users.

References

1. S. Deng, Y. Zhong, Y. Zeng, Y. Wang, X. Wang, X. Lu, X. Xia, J. Tu, Hollow TiO_2@ Co_9S_8 core-branch arrays as bifunctional electrocatalysts for efficient oxygen/hydrogen production. Adv. Sci. **5**, 1700772 (2017). https://doi.org/10.1002/advs.201700772
2. S. Deng, F. Yang, Q. Zhang, Y. Zhong, Y. Zeng et al., Phase modulation of (1T-2H)-$MoSe_2$/TiC-C shell/core arrays via nitrogen doping for highly efficient hydrogen evolution reaction. Adv. Mater. **30**, 1802223 (2018). https://doi.org/10.1002/adma.201802223
3. H. Xia, J. Zhang, Z. Yang, S. Guo, S. Guo, Q. Xu, 2D MOF nanoflake-assembled spherical microstructures for enhanced supercapacitor and electrocatalysis performances. Nano-Micro Lett. **9**(4), 43 (2017). https://doi.org/10.1007/s40820-017-0144-6
4. H. Wang, Y.-X. Yu, KOH alkalized Fe_3N nanoparticles on electrocatalytic hydrogen evolution reaction. J. Inorg. Mater. **33**(6), 653–658 (2018). https://doi.org/10.15541/jim20170350
5. M. Yu, Z. Wang, C. Hou, Z. Wang, C. Liang, C. Zhao, Y. Tong, X. Lu, S. Yang, Nitrogen-doped Co_3O_4 mesoporous nanowire arrays as an additive-free air-cathode for flexible solid-state zinc-air batteries. Adv. Mater. **29**(15), 1602868 (2017). https://doi.org/10.1002/adma.201602868
6. Q. Zhang, P. Li, D. Zhou, Z. Chang, Y. Kuang, X. Sun, Superaerophobic ultrathin Ni-Mo alloy nanosheet array from in situ topotactic reduction for hydrogen evolution reaction. Small **13**(41), 1701648 (2017). https://doi.org/10.1002/smll.201701648
7. F. Feng, J. Wu, C. Wu, Y. Xie, Regulating the electrical behaviors of 2D inorganic nanomaterials for energy applications. Small **11**(6), 654–666 (2015). https://doi.org/10.1002/smll.201402346
8. J. Li, W. Xu, J. Luo, D. Zhou, D. Zhang, L. Wei, P. Xu, D. Yuan, Synthesis of 3D hexagram-like cobalt-manganese sulfides nanosheets grown on nickel foam: a bifunctional electrocatalyst for overall water splitting. Nano-Micro Lett. **10**(1), 6 (2018). https://doi.org/10.1007/s40820-017-0160-6
9. H. Liang, L. Li, F. Meng, L. Dang, J. Zhuo, A. Forticaux, Z. Wang, S. Jin, Porous two-dimensional nanosheets converted from layered double hydroxides and their applications in electrocatalytic water splitting. Chem. Mater. **27**(27), 5702–5711 (2015). https://doi.org/10.1021/acs.chemmater.5b02177
10. M. Yu, S. Zhao, H. Feng, H. Le, X. Zhang, Y. Zeng, Y. Tong, X. Lu, Engineering thin MoS_2 nanosheets on tin nanorods: advanced electrochemical capacitor electrode and hydrogen evolution electrocatalyst. ACS Energy Lett. **2**(8), 1862–1868 (2017). https://doi.org/10.1021/acsenergylett.7b00602
11. L.L. Feng, M. Fan, Y. Wu, Y. Liu, G.D. Li, H. Chen, W. Chen, D. Wang, X. Zou, Metallic Co_9S_8 nanosheets grown on carbon cloth as efficient binder-free electrocatalysts for the hydrogen evolution reaction in neutral media. J. Mater. Chem. A **4**(18), 6860–6867 (2016). https://doi.org/10.1039/C5TA08611F
12. X. Zou, Y. Liu, G.D. Li, Y. Wu, D.P. Liu et al., Ultrafast formation of amorphous bimetallic hydroxide films on 3D conductive sulfide nanoarrays for large-current-density oxygen evolution electrocatalysis. Adv. Mater. **29**(22), 1700404 (2017). https://doi.org/10.1002/adma.201700404
13. X. Yang, J. Chen, Y. Chen, P. Feng, H. Lai, J. Li, X. Luo, Novel Co_3O_4 nanoparticles/nitrogen-doped carbon composites with extraordinary catalytic activity for oxygen evolution reaction (OER). Nano-Micro Lett. **10**(1), 15 (2017). https://doi.org/10.1007/s40820-017-0170-4
14. S. Zheng, L. Zheng, Z. Zhu, J. Chen, J. Kang, Z. Huang, D. Yang, MoS_2 nanosheet arrays rooted on hollow rgo spheres as bifunctional hydrogen evolution catalyst and supercapacitor electrode. Nano-Micro Lett. **10**(4), 62 (2018). https://doi.org/10.1007/s40820-018-0215-3
15. L. Zhu, D. Zheng, Z. Wang, X. Zheng, P. Fang, J. Zhu, M. Yu, Y. Tong, X. Lu, A confinement strategy for stabilizing ZIF-derived bifunctional catalysts as a benchmark cathode

of flexible all-solid-state zinc-air batteries. Adv. Mater. **30**, 1805268 (2018). https://doi.org/10.1002/adma.201805268

16. Z. Yu, X. Xia, S. Deng, J. Zhan, R. Fang, X. Yang, X. Wang, Z. Qiang, J. Tu, Popcorn inspired porous macrocellular carbon: rapid puffing fabrication from rice and its applications in lithium–sulfur batteries. Adv. Energy Mater. **8**(1), 1701110 (2018). https://doi.org/10.1002/aenm.201701110
17. M. Wu, S. Wang, J. Wang, Engineering $NiMo_3S_4$ |Ni_3S_2 interface for excellent hydrogen evolution reaction in alkaline medium. Electrochim. Acta **258**, 669–676 (2017). https://doi.org/10.1016/j.electacta.2017.11.112
18. J. Lv, H. Miura, Y. Meng, T. Liang, Synthesis of Ni_3S_2 nanotube arrays on nickel foam by catalysis of thermal reduced graphene for hydrogen evolution reaction. Appl. Surf. Sci. **399**, 769-774 (2016). https://doi.org/10.1016/j.apsusc.2016.12.042
19. N. Cheng, Q. Liu, A.M. Asiri, W. Xing, X. Sun, A Fe-doped Ni_3S_2 particle film as a high-efficiency robust oxygen evolution electrode with very high current density. J. Mater. Chem. A **3**(46), 23207–23212 (2015). https://doi.org/10.1039/C5TA06788J
20. C. Ouyang, X. Wang, C. Wang, X. Zhang, J. Wu, Z. Ma, S. Dou, S. Wang, Hierarchically porous Ni_3S_2 nanorod array foam as highly efficient electrocatalyst for hydrogen evolution reaction and oxygen evolution reaction. Electrochim. Acta **174**, 297–301 (2015). https://doi.org/10.1016/j.electacta.2015.05.186
21. C. Tang, Z. Pu, Q. Liu, A.M. Asiri, Y. Luo, X. Sun, Ni_3S_2 nanosheets array supported on Ni foam: A novel efficient three-dimensional hydrogen-evolving electrocatalyst in both neutral and basic solutions. Int. J. Hydrogen Energy **40**(14), 4727–4732 (2015). https://doi.org/10.1016/j.ijhydene.2015.02.038
22. Y. Su, Y. Zhang, X. Zhuang, S. Li, D. Wu, F. Zhang, X. Feng, Low-temperature synthesis of nitrogen/sulfur Co-doped three-dimensional graphene frameworks as efficient metal-free electrocatalyst for oxygen reduction reaction. Carbon **62**(5), 296–301 (2013). https://doi.org/10.1016/j.carbon.2013.05.067
23. R. Liu, D. Wu, X. Feng, K. Müllen, Nitrogen-doped ordered mesoporous graphitic arrays with high electrocatalytic activity for oxygen reduction. Angew. Chem. Int. Ed. **49**(14), 2565–2569 (2010). https://doi.org/10.1002/anie.200907289
24. W. Yang, T.P. Fellinger, M. Antonietti, Efficient metal-free oxygen reduction in alkaline medium on high-surface-area mesoporous nitrogen-doped carbons made from ionic liquids and nucleobases. J. Am. Chem. Soc. **133**(2), 206–209 (2011). https://doi.org/10.1021/ja108039j
25. J. Wang, J. Su, H. Chen, X. Zou, G.D. Li, Oxygen vacancy-rich, ru-doped In_2O_3 ultrathin nanosheets for efficient detection of xylene at low temperature. J. Mater. Chem. C **6**(15), 4165 (2018). https://doi.org/10.1039/C8TC00638E
26. L.L. Feng, G. Yu, Y. Wu, G.D. Li, H. Li, Y. Sun, T. Asefa, W. Chen, X. Zou, High-index faceted Ni_3S_2 nanosheet arrays as highly active and ultrastable electrocatalysts for water splitting. J. Am. Chem. Soc. **137**(44), 14023–14026 (2015). https://doi.org/10.1021/jacs.5b08186
27. X. Xia, S. Deng, D. Xie, Y. Wang, S. Feng, J. Wu, J. Tu, Boosting sodium ion storage by anchoring MoO_2 on vertical graphene arrays. J. Mater. Chem. A **6**(32), 15546–15552 (2018). https://doi.org/10.1039/C8TA06232C
28. Z. Yao, X. Xia, D. Xie, Y. Wang, C. Zhou, L. Sufu, S. Deng, X. Wang, J. Tu, Enhancing ultrafast lithium ion storage of $Li_4Ti_5O_{12}$ by tailored TiC/C core/shell skeleton plus nitrogen doping. Adv. Funct. Mater. **28**, 1802756 (2018). https://doi.org/10.1002/adfm.201802756
29. H. Chen, Y. Kang, F. Cai, S. Zeng, W. Li, M. Chen, Q. Li, Electrochemical conversion of $Ni_2(OH)_2CO_3$ into $Ni(OH)_2$ hierarchical nanostructures loaded on a carbon nanotube paper with high electrochemical energy storage performance. J. Mater. Chem. A **3**(5), 1875–1878 (2015). https://doi.org/10.1039/C4TA06218C
30. S. Qu, J. Huang, J. Yu, G. Chen, W. Hu, M. Yin, R. Zhang, S. Chu, C. Li, Ni_3S_2 nanosheet flowers decorated with CdS quantum dots as a highly active electrocatalysis electrode for synergistic water splitting. ACS Appl. Mater. Interfaces. **9**(35), 29660 (2017). https://doi.org/10.1021/acsami.7b06377
31. N. Jiang, Q. Tang, M. Sheng, B. You, D.E. Jiang, Y. Sun, Nickel sulfides for electrocatalytic hydrogen evolution under alkaline conditions: a case study of crystalline NiS, NiS_2, and Ni_3S_2 nanoparticles. Catal. Sci. Technol. **6**(4), 1077–1084 (2015). https://doi.org/10.1039/C5CY01111F
32. Y. Wu, Y. Liu, G.D. Li, X. Zou, X. Lian, D. Wang, L. Sun, T. Asefa, X. Zou, Efficient electrocatalysis of overall water splitting by ultrasmall $Ni_xCo_{3-x}S_4$ coupled Ni_3S_2 nanosheet arrays. Nano Energy **35**, 161–170 (2017). https://doi.org/10.1016/j.nanoen.2017.03.024
33. Z. Yao, X. Xia, Y. Zhang, D. Xie, C. Ai et al., Superior high-rate lithium-ion storage on $Ti_2Nb_{10}O_{29}$ arrays via synergistic TiC/C skeleton and N-doped carbon shell. Nano Energy **54**, 304–312 (2018). https://doi.org/10.1016/j.nanoen.2018.10.024
34. S. Shen, W. Guo, D. Xie, Y. Wang, S. Deng, Y. Zhong, X. Wang, X. Xia, J. Tu, A synergistic vertical graphene skeleton and S-C shell to construct high-performance $TiNb_2O_7$-based core/shell arrays. J. Mater. Chem. A **6**, 20195–20204 (2018). https://doi.org/10.1039/C8TA06858E
35. S. Deng, D. Chao, Y. Zhong, Y. Zeng, Z. Yao et al., Vertical graphene/$Ti_2Nb_{10}O_{29}$/hydrogen molybdenum bronze composite arrays for enhanced lithium ion storage. Energy Storage Mater. **12**, 137–144 (2018). https://doi.org/10.1016/j.ensm.2017.11.018
36. C. Zhang, Y. Zhou, Y. Zhang, S. Zhao, J. Fang, X. Sheng, T. Zhang, H. Zhang, Double-shelled TiO_2 hollow spheres assembled with TiO_2 nanosheets. Chemistry **23**(18), 4336–4343 (2017). https://doi.org/10.1002/chem.201602654
37. C. Wang, Y. Zhan, Z. Wang, TiO_2, MoS_2, and TiO_2/MoS_2 heterostructures for use in organic dyes degradation. ChemistrySelect **3**(6), 1713–1718 (2018). https://doi.org/10.1002/slct.201800054
38. Y. Zhang, X. Xia, X. Cao, B. Zhang, N.H. Tiep et al., Ultrafine metal nanoparticles/N-doped porous carbon hybrids coated on carbon fibers as flexible and binder-free water splitting

catalysts. Adv. Energy Mater. **7**, 1700220 (2017). https://doi.org/10.1002/aenm.201700220

39. B. Liu, Y. Wang, H. Peng, R. Yang, Z. Jiang, X. Zhou et al., Feroxyhyte nanosheets: iron vacancies induced bifunctionality in ultrathin feroxyhyte nanosheets for overall water splitting. Adv. Mater. **30**, 1803144 (2018). https://doi.org/10.1002/adma.201803144
40. B. Liu, H. Peng, Y. Zhao, J. Cheng, J. Xia, J. Shen et al., Unconventional nickel nitride enriched with nitrogen vacancies as a high-efficiency electrocatalyst for hydrogen evolution. Adv. Sci. **5**, 1800406 (2018). https://doi.org/10.1002/advs.201800406
41. B. Liu, J. Cheng, H.Q. Peng, D. Chen, X. Cui et al., In situ nitridated porous nanosheet networked Co_3O_4–Co_4N heteronanostructures supported on hydrophilic carbon cloth for highly efficient electrochemical hydrogen evolution. J. Mater. Chem. A **7**, 775–782 (2019). https://doi.org/10.1039/C8TA09800J
42. Y. Huang, H. Lu, H. Gu, J. Fu, S. Mo, C. Wei, Y.-E. Miao, T. Liu, A CNT@$MoSe_2$ hybrid catalyst for efficient and stable hydrogen evolution. Nanoscale **7**(44), 18595–18602 (2015). https://doi.org/10.1039/C5NR05739F
43. Z. Peng, D. Jia, A.M. Al-Enizi, A.A. Elzatahry, G. Zheng, Electrocatalysts: from water oxidation to reduction: homologous Ni–Co based nanowires as complementary water splitting electrocatalysts. Adv. Energy Mater. **5**(9), 1402031 (2015). https://doi.org/10.1002/aenm.201402031
44. Y.P. Zhu, T.Y. Ma, M. Jaroniec, S.Z. Qiao, Self-templating synthesis of hollow Co_3O_4 microtube arrays for highly efficient water electrolysis. Angew. Chem. Int. Ed. **56**(5), 1324–1328 (2016). https://doi.org/10.1002/anie.201610413
45. J. Tian, N. Cheng, Q. Liu, W. Xing, X. Sun, Cobalt phosphide nanowires: efficient nanostructures for fluorescence sensing of biomolecules and photocatalytic evolution of dihydrogen from water under visible light & dagger. Angew. Chem. Int. Ed. **54**(18), 5493–5497 (2015). https://doi.org/10.1002/ange.201501237
46. L. Feng, F. Song, X. Hu, Ni_2P as a janus catalyst for water splitting: the oxygen evolution activity of Ni_2P nanoparticles. Energy Environ. Sci. **8**(8), 2347–2351 (2015). https://doi.org/10.1039/C5EE01155H
47. M. Ledendecker, C.S. Krick, C. Papp, H.P. Steinrück, M. Antonietti, M. Shalom, The synthesis of nanostructured Ni_5P_4 films and their use as a non-noble bifunctional electrocatalyst for full water splitting. Angew. Chem. Int. Ed. **54**(42), 12361–12365 (2015). https://doi.org/10.1002/anie.201502438

 https://doi.org/10.1007/s40820-019-0242-8